


## Article

# Modelling and Control of Thermal Stress in TSLAG ( $\text{Tb}_3\text{Sc}_{1.95}\text{Lu}_{0.05}\text{Al}_3\text{O}_{12}$ ) Magneto-Optical Crystals Grown by Czochralski Method

Junling Ding <sup>1,2,\*</sup> , Yu Zhang <sup>1</sup>, Yuankai Hao <sup>2</sup> and Xiuwei Fu <sup>2</sup><sup>1</sup> School of Mechatronics and Vehicle Engineering, East China Jiaotong University, Nanchang 330013, China<sup>2</sup> State Key Laboratory of Crystal Materials, Shandong University, Jinan 250100, China

\* Correspondence: jlding@ecjtu.edu.cn

**Abstract:**  $\text{Tb}_3\text{Sc}_{1.95}\text{Lu}_{0.05}\text{Al}_3\text{O}_{12}$  (TSLAG) crystals are novel and high-quality magneto-optical materials with the most promising application as the core component of Faraday devices. Cracking is an obstacle to TSLAG crystal growth and is closely influenced by crystal thermal stress distribution. In this work, the evolution of thermal stress during TSLAG crystal growth in the initial Czochralski (Cz) furnace is numerically studied. The reasons for high thermal stress in TSLAG crystal are explained based on the results about the melt flow, the temperature distribution in the furnace, and the crystal/melt interface shape. A large crucible with a shallow melt is proposed to address the problem of significant variations in melt depth during TSLAG crystal growth. Based on the numerical results, the proposed design can stabilize the melt flow structure, suppressing changes in the crystal/melt interface shape and effectively improving thermal stress in the TSLAG crystal growth process, which contributes to precisely regulating the preparation of large-sized high-quality TSLAG crystals.

**Keywords:** TSLAG crystal; Czochralski method; thermal stress; melt flow; interface shape



**Citation:** Ding, J.; Zhang, Y.; Hao, Y.; Fu, X. Modelling and Control of Thermal Stress in TSLAG ( $\text{Tb}_3\text{Sc}_{1.95}\text{Lu}_{0.05}\text{Al}_3\text{O}_{12}$ ) Magneto-Optical Crystals Grown by Czochralski Method. *Crystals* **2024**, *14*, 564. <https://doi.org/10.3390/cryst14060564>

Academic Editor: Raphaël P. Hermann

Received: 11 May 2024

Revised: 12 June 2024

Accepted: 12 June 2024

Published: 18 June 2024



**Copyright:** © 2024 by the authors. Licensee MDPI, Basel, Switzerland. This article is an open access article distributed under the terms and conditions of the Creative Commons Attribution (CC BY) license (<https://creativecommons.org/licenses/by/4.0/>).

## 1. Introduction

With the development of high-power laser and optical communication technology, magneto-optical isolators have been increasingly studied and applied, promoting the rapid development of magneto-optical crystals [1]. In order to meet the growing demands for visible and near-infrared laser diodes and fibre lasers, it is necessary to continuously improve the size and optical performance of magneto-optical crystals. Currently, the terbium-containing garnet crystals, including terbium aluminium garnet (TAG), terbium scandium aluminium garnet (TSAG), and terbium gallium garnet (TGG) crystals, have been the subject of extensive research and applications in the field of magneto-optical crystals [2–4]. Among them, TGG crystals have the broadest research scope and are the most mature magneto-optical crystals in commercial applications. However, the gallium volatilization and growth spiral issues in the TGG crystal growth process limit the growth of large-sized crystals [5,6]. Researchers have recently found that compared to TGG crystals, the improved crystal  $\text{Tb}_3\text{Sc}_{1.95}\text{Lu}_{0.05}\text{Al}_3\text{O}_{12}$  (TSLAG) of TSAG exhibits several advantages, including a lower absorption coefficient, a larger Verdet constant, a greater resistance to the laser damage threshold, and an ease of crystal growth [7–9]. Therefore, TSLAG crystals are expected to replace TGG crystals in the field of magneto-optical crystals, emerging as novel and high-quality magneto-optical crystals with the most promising prospects for future applications.

The techniques used for growing magneto-optical crystals include the Czochralski (Cz) method, the optical floating zone method, the flux method, etc. Among the above methods, the Cz method uses seed crystals to overcome the drawback of excessive spontaneous nucleation. At the same time, due to the stirring effect induced by seed crystal rotation, the crystal grows faster, and the number of wrapped defects is reduced. Currently, these are widely used in the preparation of large-sized magneto-optical crystals, due to their

effectiveness in mitigating nucleation issues and promoting faster and more controlled crystal growth. In terms of TSLAG magneto-optical crystal growth, Shimamura et al. [10,11] originally doped a small amount of Lu element in the process of preparing TSAG crystals, and successfully employed the Cz technique to grow a 2-inch TSLAG single crystal and conducted a detailed analysis of its optical and magneto-optical properties. Their research found that the introduction of Lu element is beneficial for the uniformity and stability of crystal growth. TSLAG crystals produce a Faraday rotation comparable to TAG crystals and exhibit excellent transparency in the visible-light band. More recently, Tao et al. [7] explored the preparation of bulk TSLAG crystals by the Cz method and systematically measured their thermal and optical properties, providing important reference data for their application in the strong lasers. And a large-size TSLAG crystal with a diameter of 65 mm was grown by Zhang et al. [9] by optimizing the technology of the crystal growth process and through raw material preparation, and a detailed comparison was carried out between the physical properties of TSLAG and other magneto-optical crystals.

However, in the preparation process of magneto-optical crystals, cracking is an obstacle to crystal growth, which is closely influenced by the distribution of thermal stress in the crystal. Aiming at obtaining bulk high-quality TSLAG crystals, the regulation of thermal stress in crystals is a particularly important issue. Thus, it is necessary to optimize the thermal field structure and growth process of TSLAG magneto-optical crystal to obtain a thermal stress distribution favourable for crystal growth. In the present work, the crystal thermal stress distribution during the CZ growth of bulk TSLAG magneto-optical crystals was investigated using a 2D numerical model. The causes of high thermal stress in the TSLAG crystal using the current Cz furnace were examined in detail. And a scheme for reducing thermal stress in TSLAG magneto-optical crystals has been proposed.

## 2. Modelling Approach

### 2.1. Description of Experimental Setup

The induction-heating Cz furnace for growing TSLAG magneto-optical crystals consists of an iridium crucible, TSLAG melt and crystal, a zirconia insulator, a copper induction coil, a stainless steel chamber, and high-purity argon gas. Figure 1 shows a schematic diagram of an induction-heating Cz furnace. The raw materials are mixed and melted in an iridium crucible with a diameter of 60 mm, a height of 60 mm, and a thickness of 2 mm [7]. The initial melt depth is set at 50 mm. The TSLAG crystal diameter is 30 mm. During Cz furnace operation, we introduce an alternating current in the copper induction coils to induce heat generation in the iridium crucible. The current frequency is 7 kHz. Additionally, the crystal pulling speed is maintained at 1.0 mm/h. The physical properties of primary component materials are listed in in Table 1 [7,12].

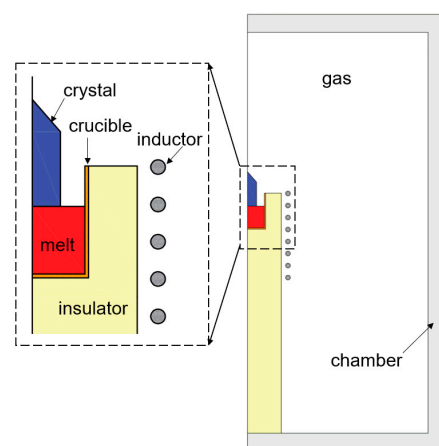


**Figure 1.** A schematic of the Cz furnace for growing TSLAG crystals.

**Table 1.** Physical properties of main materials.

Material	Variable	Value
TSLAG melt	Density (kg/m <sup>3</sup> )	5600
	Thermal conductivity (W/m·K)	7.6
	Heat capacity (J/kg·K)	1881
	Dynamic viscosity (kg/m·s)	0.06
	Melting point (K)	2173
	Thermal expansion (1/K)	$7.23 \times 10^{-5}$
TSLAG crystal	Emissivity	0.6
	Density (kg/m <sup>3</sup> )	5835
	Thermal conductivity (W/m·K)	5.64
	Heat capacity (J/kg·K)	451
	Emissivity	0.6
	Thermal expansion (1/K)	$7.23 \times 10^{-6}$
Iridium	Poisson ratio	0.273 <sup>a</sup>
	Young's modulus	$1.3 \times 10^{11}$ <sup>a</sup>
	Density (kg/m <sup>3</sup> )	22,400
	Thermal conductivity (W/m·K)	147
	Heat capacity (J/kg·K)	130
	Emissivity	0.5
Zirconia	Permeability(H/m)	$1.2566 \times 10^{-6}$
	Electrical conductivity (S/m)	$1.8868 \times 10^7$
	Density (kg/m <sup>3</sup> )	6040
	Thermal conductivity (W/m·K)	2.14
	Heat capacity (J/kg·K)	419
	Emissivity	0.4

<sup>a</sup> These values refer to the physical properties of silicon, as silicon crystal also belongs to the cubic system.

## 2.2. Temperature and Velocity Fields

Since both the Cz furnace and the main components are symmetrical in the circumferential direction, a two-dimensional axisymmetric simplification is adopted for the growth system. And some assumptions are used in the numerical modelling: (1) TSLAG melt is comprised of incompressible Newtonian fluids, and the Boussinesq assumption is adopted to calculate the thermal buoyancy; (2) argon behaves as an ideal gas, approximated at low Mach numbers; (3) we ignore the absorption of radiation energy by argon gas, and all radiation surfaces in the furnace are diffuse grey surfaces; and (4) given the slow crystal growth rate of 1 mm/h, the system is in a quasi-steady state.

The heat transfer and fluid flow in each region meet the conditions of mass conservation, momentum conservation, and energy conservation. The corresponding expressions are as follows:

In the melt:

$$\nabla \cdot \vec{u}_m = 0 \quad (1)$$

$$\rho_m \vec{u}_m \cdot \nabla \vec{u}_m = -\nabla \cdot p_m + \nabla \cdot (\mu_{m,eff} \nabla \cdot \vec{u}_m) + \rho_m \vec{g} \beta_T (T_m - T_{ref}) \quad (2)$$

$$\rho_m C_{p,m} \vec{u}_m \nabla T_m = \lambda_m \nabla \cdot \nabla T \quad (3)$$

In the argon gas:

$$\nabla \cdot (\rho_g \vec{u}_g) = 0 \quad (4)$$

$$\nabla \cdot (\rho_g \vec{u}_g \vec{u}_g) = -\nabla \cdot p_g + \nabla \cdot \left( -\frac{2}{3} \mu_{g,eff} \nabla \cdot \vec{u}_g \right) + \nabla \cdot (2\mu_{g,eff} S_g) + (\rho_g - \rho_0) \vec{g} \quad (5)$$

$$\nabla \cdot (\rho_g C_{p,g} \vec{u}_g T_g) = \nabla \cdot (\lambda_g \nabla T_g) \quad (6)$$

$$\rho_g = p_g / R_g T_g \quad (7)$$

In the solid components:

$$\nabla \cdot (\lambda_s \nabla T_s) + Q_h = 0 \quad (8)$$

where subscripts  $m$ ,  $g$ , and  $s$  represent TSLAG melt, argon gas, and solid components, respectively.  $\vec{u}$ ,  $\rho$ ,  $p$ ,  $\mu_{eff}$ ,  $C_p$ ,  $T$ , and  $\lambda$  are the velocity vector, density, pressure, effective viscosity coefficient, heat capacity, temperature, and thermal conductivity, respectively.  $\vec{g}$  is the gravitational acceleration vector.  $\beta$  is the thermal expansion coefficient of TSLAG melt, and  $R_g$  is the specific gas constant.  $Q_h$  is the heat generated by electromagnetic induction, which only exists in the iridium crucible. In our present work, the heating power density is calculated via ANSYS Maxwell 15.0 software.

The net radiation method is employed to calculate the heat transfer via radiation:

$$\frac{q(\vec{x})}{\varepsilon(\vec{x})} - \int_{\vec{x} \in \partial V} K(\vec{x}, \vec{x}^*) \frac{1 - \varepsilon(\vec{x}^*)}{\varepsilon(\vec{x}^*)} q(\vec{x}^*) dS^* = \sigma T^4(\vec{x}) - \int_{\vec{x}^* \in \partial V} K(\vec{x}, \vec{x}^*) \sigma T^4(\vec{x}^*) dS^* \quad (9)$$

where  $q(\vec{x})$  and  $\varepsilon(\vec{x})$  are the net heat flux and surface emissivity, respectively.  $\vec{x}$  and  $\vec{x}^*$  are the radiation microelements in radiation space  $\partial V$ , and  $K(\vec{x}, \vec{x}^*)$  is the surface view factor, while  $dS^*$  is the area of the radiation microelement, and  $\sigma$  is the Stefan–Boltzmann constant.

### 2.3. Thermal Stress

The stress in TSLAG crystal is as follows:

$$\partial \sigma_{ij} / \partial x_j = 0 \quad (10)$$

Considering the elastic strain and thermal strain due to the temperature change in the crystal, the stress–strain relationship is shown as the following:

$$\sigma_{ij} = C_{ijkl} (\varepsilon_{kl} - \alpha (T - T_0) \delta_{kl}) \quad (11)$$

where  $C_{ijkl}$  and  $\alpha$  are the elastic and thermal expansion coefficients of TSLAG crystal, respectively.  $\delta_{kl}$  represents the Kronecker delta tensor.  $T_0$  is the reference temperature for calculating the thermal stress in TSLAG crystal.

Considering that TSLAG crystals are classified as having a cubic system, and the Cz crystals have a cylindrically symmetric shape [7,8], Equation (11) in a cylindrical coordinate system is summarised as follows [13]:

$$\begin{bmatrix} \sigma_{rr} \\ \sigma_{\theta\theta} \\ \sigma_{zz} \\ \sigma_{rz} \end{bmatrix} = \frac{E}{(1 + \gamma)(1 - 2\gamma)} \begin{bmatrix} 1 - \gamma & \gamma & \gamma \\ \gamma & 1 - \gamma & \gamma \\ \gamma & \gamma & 1 - \gamma \\ 1 - 2\gamma & & \end{bmatrix} \begin{bmatrix} \varepsilon_{rr} - \alpha(T - T_0) \\ \varepsilon_{\theta\theta} - \alpha(T - T_0) \\ \varepsilon_{zz} - \alpha(T - T_0) \\ \varepsilon_{rz} \end{bmatrix} \quad (12)$$

where  $\gamma$  and  $E$  are the Poisson ratio and Young's modulus of TSLAG crystals, respectively.

The strain's  $\varepsilon_{ij}$  is connected with the radial displacement  $u$  and the axial displacement  $v$  in the crystal as shown below:

$$\varepsilon_{rr} = \frac{\partial u}{\partial r}, \quad \varepsilon_{\theta\theta} = \frac{u}{r}, \quad \varepsilon_{zz} = \frac{\partial v}{\partial z}, \quad \varepsilon_{rz} = \frac{\partial u}{\partial z} + \frac{\partial v}{\partial r} \quad (13)$$

As for the evaluation of crystal stress, Von Mises stress is more suitable for analysing dislocations and crystal cracking, which are shown as follows:

$$\sigma_{Mises} = \sqrt{\frac{(\sigma_{rr} - \sigma_{zz})^2 + (\sigma_{\theta\theta} - \sigma_{rr})^2 + (\sigma_{\theta\theta} - \sigma_{zz})^2 + 6\sigma_{rz}^2}{2}} \quad (14)$$

## 2.4. Computational Method and Boundary Conditions

No-slip conditions are applied to all solid walls in contact with the fluid domains. Temperature continuity and heat flux conservation at all internal boundaries are maintained. The furnace outer wall temperature is maintained at 300 K. Specifically, the Stefan condition is satisfied at the crystal/melt (c-m) interface considering the latent heat release:

$$k_s \nabla T_s - k_m \nabla T_m = \rho_s \Delta H V_n \quad (15)$$

where  $k$  is the thermal conductivity and subscripts  $s$  and  $m$  represent TSLAG crystal and melt, respectively.  $\Delta H$  is the latent heat of TSLAG crystal crystallization, and  $V_n$  is the crystal growth rate.

As for the thermal stress calculation, a zero-displacement condition is imposed on the central axis and bottom centre point of the TSLAG crystal region. Additionally, the remaining crystal walls are left unconstrained. And the algorithms for solving the temperature and velocity fields in the Cz furnace have been presented in Refs. [14,15].

## 3. Results and Discussion

### 3.1. Heat Transfer in the Furnace

Utilizing the developed computational model, we investigated the global temperature distribution in the Cz furnace for TSLAG crystal growth, as displayed in Figure 2a. It is obvious that the high-temperature areas in the furnace are primarily concentrated in the crystal growth regions. Thus, it can be assumed that the small asymmetric structure of the furnace wall has a minimal impact on the temperature distribution in the crystal growth region. Additionally, the iridium crucible serves as the primary heat source in the furnace. The distribution of heating power density in the iridium crucible is shown in Figure 2b. Clearly, due to the skin effect, induction heating power is concentrated in the vicinity of the crucible outer wall, with its maximum value located at the crucible corner. This is because this position is close to the vertical centre of the induction coil. However, under the influence of the global heat transfer in the Cz furnace, the temperature on the crucible sidewall is lower than that at the bottom of the crucible, despite its larger heating power density. And the highest temperature distribution occurs at the corner of the iridium crucible.

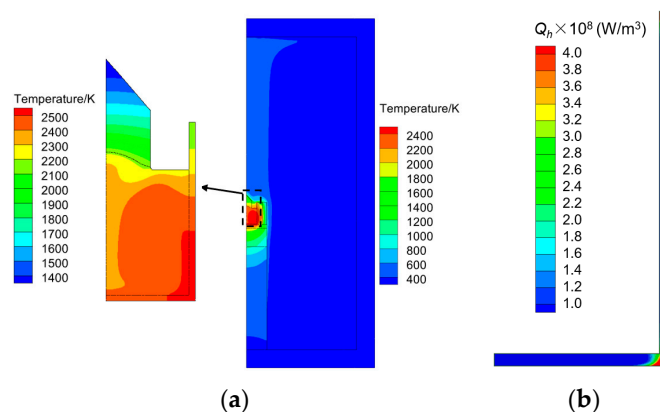


**Figure 2.** Distributions of temperature in the furnace (a) and heating power per unit volume in the iridium crucible (b) under the condition of the original thermal field structure.

### 3.2. Melt Temperature and Flow

The crystal quality grown by the melt method is closely related to the flow and temperature distribution in the melt region, especially near the c-m interface. And TSLAG crystal rotation is typically applied to adjust the growth process. Additionally, the melt depth gradually decreasing due to the continuous pulling of crystals from the melt. Thus, to reveal the evolution process of melt temperature and flow during TSLAG growth, three different crystal rotation speeds and five crystal heights were considered, as shown in Figure 3.

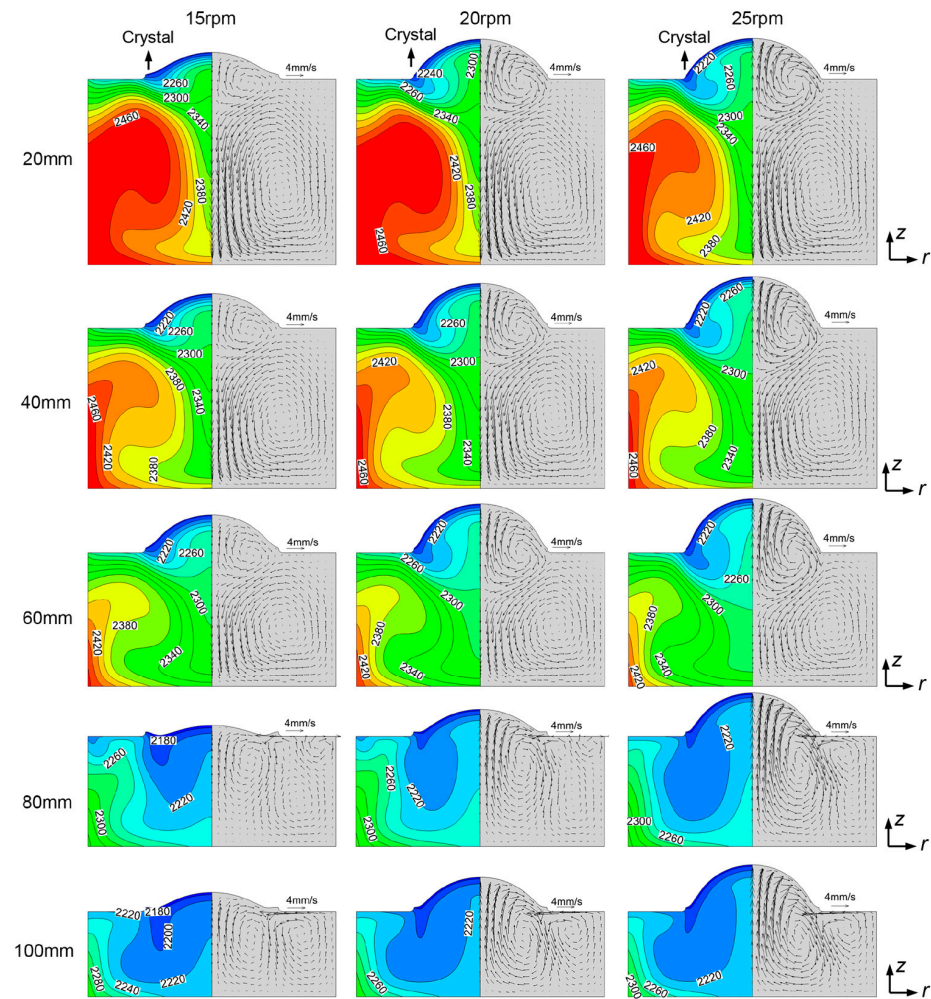


**Figure 3.** Distributions of melt flow and temperature fields during TSLAG crystal growth at different crystal rotation speeds. The crystal heights are 20 mm, 40 mm, 60 mm, 80 mm, and 100 mm, respectively. The reference speed marked in the figure is 4 mm/s.

During the TSLAG crystal growth, various internal forces, such as the thermal buoyancy caused by the melt temperature difference in the axial direction, the surface tension induced by the temperature difference on the melt-free surface, and the centrifugal forces influenced by crystal rotation, are present, with thermal buoyancy being the primary driving force. As depicted in Figure 3, influenced by thermal buoyancy-driven natural convection and crystal rotation, when the melt depth is substantial, two vortices are observed in the melt: an anticlockwise vortex close to the bottom of the crucible and a clockwise vortex beneath the TSLAG crystal. Notably, the thermal buoyancy vortex occupies the majority of the melt area. As the crystal rotation speed increases, the natural convection is inhibited, and the area occupied by the thermal buoyancy vortex gradually decreases. Conversely, it is evident that as the crystal rotation speed increases, the melt velocity beneath the crystal increases, and the clockwise flow strengthens, manifested by the expansion of its occupied area. It should be pointed out that the clockwise flow beneath the crystal hinders the attainment of a flat c-m interface [16]. Therefore, the improvement in crystal speed is not conducive to obtaining a flat c-m interface in the present study. However, when the melt is shallow, significant changes occur in the melt flow. The thermal buoyancy vortex is compressed towards the crucible's sidewall, and the clockwise vortex induced by crystal rotation dominates the primary melt area.

As for the melt temperature distribution, thermal plumes induced by natural convection are prominently observed in the vicinity of the crucible sidewall. Simultaneously, the crucible



wall temperature, as well as the melt temperature, decreases with a reduction in melt depth. This is attributed to the iridium crucible serving as the heat source in the melt. As the melt depth decreases, the thermal resistance from the high-temperature crucible wall to the c-m interface diminishes. Additionally, the crystal gradually penetrates into the crucible, and the high-temperature crucible insulates the crystal and the melt. Consequently, the heat loss through the crystal surface and the melt-free surface reduces with a decrease in the melt depth. And when the melt depth is high, significant temperature gradients are observed beneath the c-m interface, indicating that more heat is transmitted into TSLAG crystals.

### 3.3. Thermal Stress

The cracking of TSLAG crystals is closely related to the distribution of thermal stress in the crystal. In order to obtain large-sized, high-quality TSLAG crystals, the factor analysis of influencing crystal thermal stress is an important concern. Figure 4 illustrates the distribution of temperature and thermal stress in the crystal during the TSLAG crystals' growth at different crystal rotation speeds. It can be observed that the temperature of the crystal head gradually decreases with the increase in crystal height. In addition, at the same horizontal position of the crystal, the crystal temperature is generally identical. As for the thermal stress, the maximum thermal stress is concentrated near the c-m interface for crystal heights of 20 mm, 40 mm, and 60 mm at all three crystal rotation speeds. Additionally, the same trend occurs in the later stages of crystal growth (crystal heights of 80 mm and 100 mm) at crystal rotation speeds of 20 rpm and 25 rpm. However, when the crystal rotation speed is 15 rpm, the maximum thermal stress is concentrated near the crystal sidewall in the later stages of crystal growth. It should be noted that, in all conditions except for the 20 mm crystal height, the thermal stress in the TSLAG crystal region, excluding the vicinity of the c-m interface, is concentrated at the same horizontal position and does not vary with changes in crystal height. This indicates that the crystal thermal stress is closely related to the position of TSLAG crystal relative to the thermal field structure in the furnace, especially the iridium crucible, that encloses the crystal.

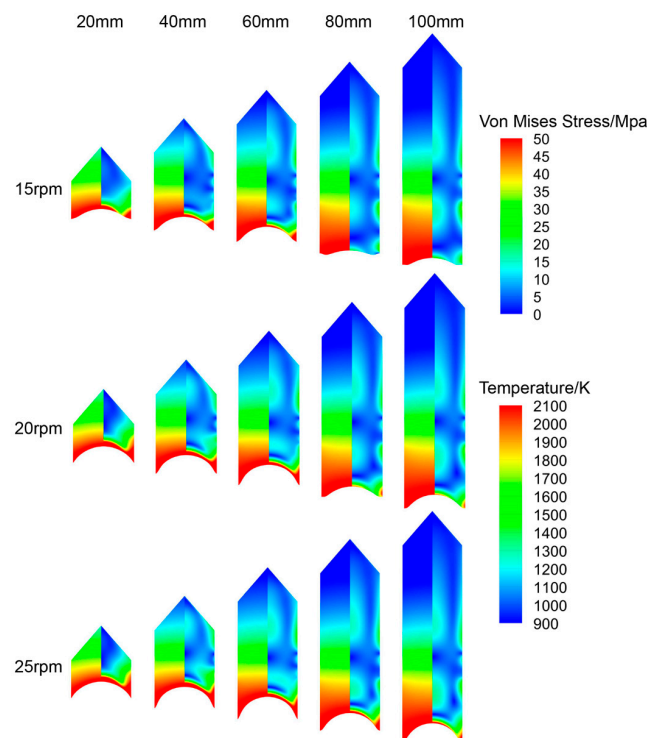


**Figure 4.** Distributions of temperature (left) and thermal stress (right) in the crystal during TSLAG crystal growth at different crystal rotation speeds. The crystal heights are 20 mm, 40 mm, 60 mm, 80 mm, and 100 mm, respectively.

### 3.4. Interface Shape

The c-m interface shape in the CZ crystal growth process not only affects the radial distribution uniformity of impurities in the crystal but also influences the crystal thermal stress near the interface. A flat interface is beneficial for improving the radial uniformity of impurities' and dopants' distribution, while simultaneously reducing thermal stress in the crystal. Our research reveals that, at different crystal rotation speeds, during the early stage of crystal growth (crystal heights of 20 mm, 40 mm, and 60 mm), the interface gradually becomes concave as the crystal height increases, as shown in Figure 5. In the later stages of crystal growth (crystal heights of 80 mm and 100 mm), a noticeable variation in the c-m interface occurs due to the significant changes in the melt flow structure, as shown in Figure 3. When the crystal height is 80 mm, the interface undergoes a significant improvement. However, as the crystal height continues to increase, the interface becomes concave again. Therefore, it can be concluded that under stable melt flow structure conditions, the concavity of c-m interface increases continuously in the TSLAG crystal growth process. Moreover, for the same crystal height, a higher crystal rotation speed leads to a greater concavity of the c-m interface, which has been reported in studies on Cz crystal growth [17,18].

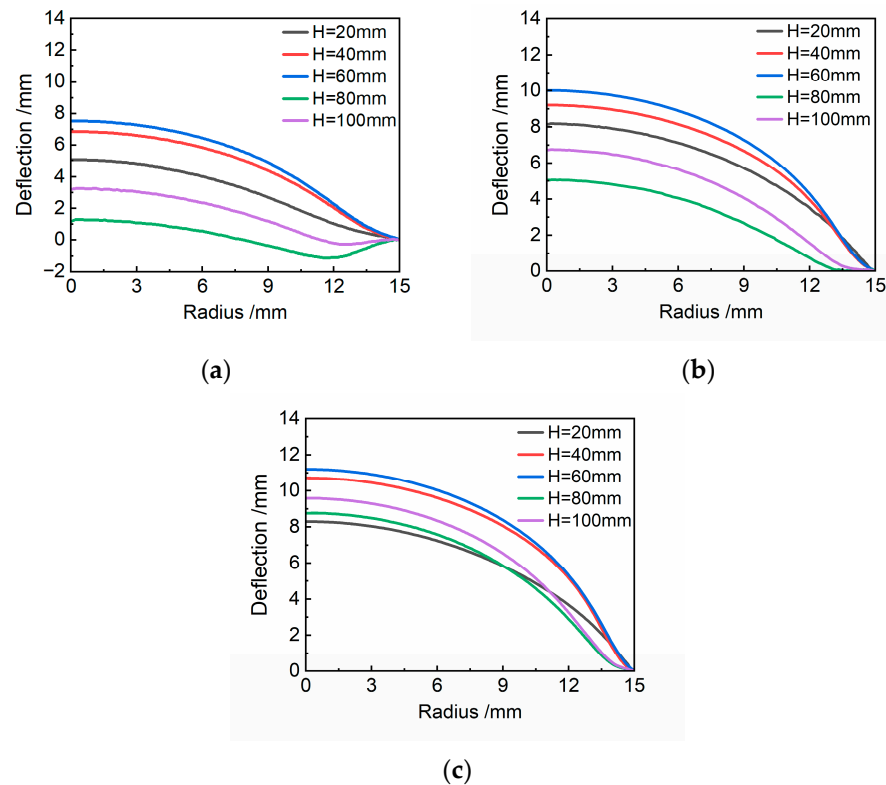


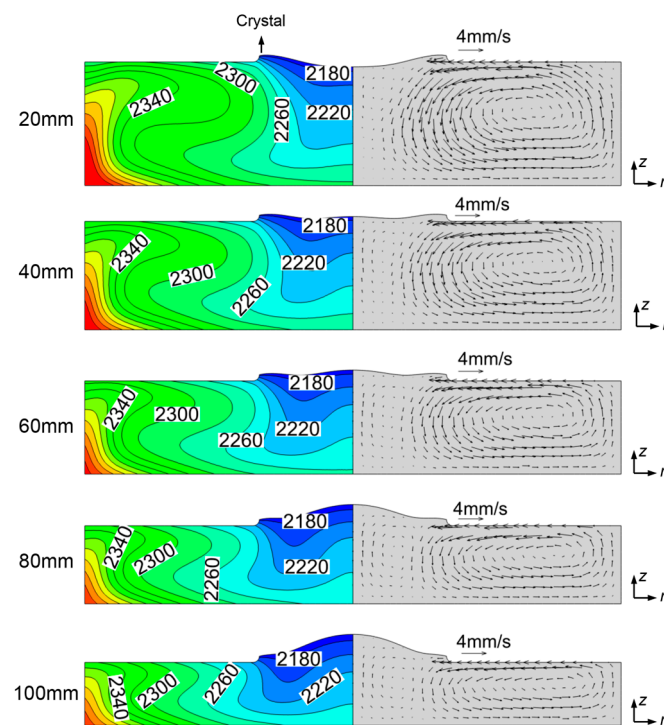
**Figure 5.** Variations in c-m interface shape during TSLAG crystals' growth (crystal heights are 20 mm, 40 mm, 60 mm, 80 mm, and 100 mm, respectively) at different crystal rotation speeds. (a) 15 rpm. (b) 20 rpm. (c) 25 rpm.

### 3.5. Improving Thermal Field Structure

Based on the analysis in the above sections, it is evident that the melt flow, melt temperature, crystal thermal stress, and c-m interface shape are closely related to the melt depth in the iridium crucible. In the initial crucible design, significant variations in melt depth during the TSLAG crystal growth led to changes in the melt flow structure, resulting in inconsistent patterns of crystal thermal stress and interface shape with respect to crystal height. This inconsistency poses challenges for the precise control of crystal growth and the preparation of high-quality crystals. Furthermore, the relative position of the melt-free surface against the iridium crucible significantly influences the thermal stress in TSLAG crystal.

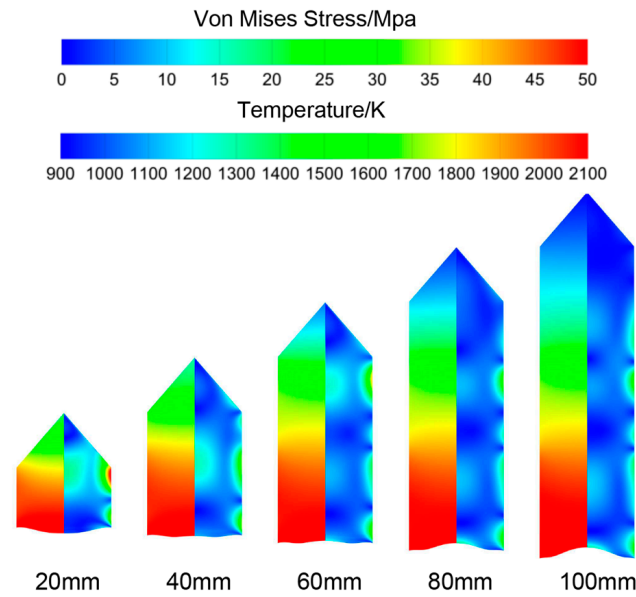


Therefore, this study uses a large crucible with a shallow melt thermal field structure for TSLAG crystal preparation. The crucible diameter is set at 90 mm, and the crystal rotation speed is maintained at 15 rpm. Figure 6 illustrates the melt flow patterns and temperature distributions at different stages of TSLAG crystal growth using the proposed thermal field structure. It can be observed that the melt flow pattern in the iridium crucible remains stable in the TSLAG crystal growth process. The counter-clockwise vortex induced by thermal buoyancy dominates the majority of the melt region, causing the melt to move along the crucible sidewall from the bottom of the crucible, then passing through the melt-free surface and beneath the crystal, and finally returning to the bottom of the crucible. Simultaneously, the clockwise vortex induced by crystal rotation consistently persists beneath the crystal. As the crystal continues to be pulled, the melt volume in the crucible gradually decreases, and the flow induced by crystal rotation intensifies, but without affecting the overall flow structure. Additionally, by comparing Figure 3 with Figure 6, it can be seen that when the large crucible with a shallow melt structure is adopted, the melt temperature distribution remains relatively constant, and there is a minor variation in melt temperature difference in the TSLAG crystal growth process.



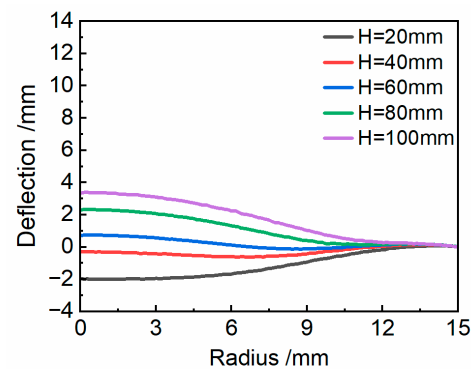
**Figure 6.** Distributions of melt flow and temperature fields during TSLAG crystal growth when the large crucible with a shallow melt structure is used. The crystal heights are 20 mm, 40 mm, 60 mm, 80 mm, and 100 mm, respectively. The reference speed marked in the figure is 4 mm/s.

Figure 7 illustrates the distribution of temperature and thermal stress in the TSLAG crystal at different growth stages when employing the large crucible with a shallow melt structure. It is obvious that the maximum crystal thermal stress during the TSLAG crystal growth is always distributed on the crystal sidewalls. Compared with the thermal stress results before improving the thermal field structure in Figure 4, the utilization of a large crucible with a shallow melt significantly reduces the thermal stress in TSLAG crystal, particularly and significantly improving the thermal stress near the c-m interface. In addition, the thermal stress in the crystal central region is also effectively reduced. Furthermore, in the early stage of crystal growth (a crystal height of 20 mm), the maximum thermal stress is primarily concentrated near the shoulder of the crystal, as shown in Figure 7.



**Figure 7.** Distributions of temperature (left) and thermal stress (right) in the crystal during TSLAG crystal growth when a large crucible with a shallow melt structure is used. The crystal heights are 20 mm, 40 mm, 60 mm, 80 mm, and 100 mm, respectively.

The c-m interface shape at different stages of TSLAG crystal growth when employing the improved thermal field structure is shown in Figure 8. It is obvious that the c-m interface gradually becomes concave with increasing crystal height in the TSLAG crystal growth process. In comparison with the interface shapes before improving the thermal field structure, the interface deflection is smaller, and the overall interface deflection range is reduced when using a large crucible with a shallow melt. And the evolution of the interface shape with respect to crystal height is stable rather than sudden, which contributes to the precise regulation of the preparation of high-quality TSLAG crystals.



**Figure 8.** Variations in c-m interface shape during TSLAG crystal growth (crystal heights are 20 mm, 40 mm, 60 mm, 80 mm, and 100 mm, respectively) when a large crucible with a shallow melt structure is adopted.

#### 4. Conclusions

In our present work, we found that in the original crucible design for TSLAG crystal growth, there is a significant variation in melt depth due to the continuous pulling of the crystals from the melt. Changes in the melt flow structure occur in both the early and late stages of crystal growth, leading to inconsistencies in the patterns of crystal thermal stress and interface shape with respect to crystal height. This situation poses a challenge for controlling crystal growth, thereby hindering the preparation of high-quality crystals. Additionally, the position of the melt-free surface relative to the iridium crucible

significantly influences the thermal stress distribution in the crystal. Then, we proposed the use of a large crucible with a shallow melt design to mitigate the problem of significant variations in melt depth during TSLAG crystal growth. Based on the numerical results, we found that the improved design stabilizes the melt flow structure, effectively improving crystal thermal stress and simultaneously suppressing changes in the c-m interface shape.

**Author Contributions:** Conceptualization, J.D. and X.F.; methodology, J.D.; software, Y.H. and X.F.; validation, J.D.; investigation, J.D. and Y.Z.; writing—original draft preparation, Y.Z.; writing—review and editing, J.D.; supervision, X.F.; funding acquisition, J.D. All authors have read and agreed to the published version of the manuscript.

**Funding:** This research was funded by the Jiangxi Provincial Natural Science Foundation (grant number 20224BAB204052), the State Key Laboratory of Crystal Materials, Shandong University (grant number KF21-11), and the Key R&D Plan of Jiangxi Province (grant number 20223BBE51026).

**Data Availability Statement:** The data that support the findings of this study are available from the corresponding author upon reasonable request.

**Conflicts of Interest:** The authors declare no conflicts of interest.

## References

1. Wang, Y.; Xu, B.G.; Zhang, D.G.; Xu, S.X.; Dong, Z.; Zeng, X.K.; Lu, X.W.; Pei, J.H. Magneto-Optical Isolator Based on Ultra-Wideband Photonic Crystals Waveguide for 5G Communication System. *Crystals* **2019**, *9*, 570. [[CrossRef](#)]
2. Zhang, H.T.; Dou, R.Q.; Zhang, Q.L.; Liu, W.P.; Sun, G.H.; Luo, J.Q. Research progress and applications of magneto-optical crystal. *J. Synth. Cryst.* **2020**, *49*, 346–357.
3. Wang, F.; Wu, Y.H.; Xu, X.M.; Zhang, R.; Luo, Q.; Lu, H.; Wang, S.H.; Wu, S.F. Preparation and properties of novel  $(\text{Tb}_{1-x}\text{Ce}_x)_3\text{Sc}_2\text{Al}_3\text{O}_{12}$  magneto-optical transparent ceramics with different doping concentrations. *CrystEngComm* **2023**, *25*, 3171. [[CrossRef](#)]
4. Ivanov, I.A.; Karimov, D.N.; Snetkov, I.L.; Palashov, O.V.; Kochurikhin, V.V.; Masalov, A.V.; Fedorov, V.A.; Ksenofontov, D.A.; Kabalov, Y.K. Study of the influence of Tb-Sc-Al garnet crystal composition on Verdet constant. *Opt. Mater.* **2017**, *66*, 106–109. [[CrossRef](#)]
5. Chen, J.B.; Lin, Y.; Li, G.H.; Chen, J.S.; Teng, S.; Yao, Y.G. Growth of Large-size and High-quality TGG Crystal by Automatic Czochralski Method. *J. Synth. Cryst.* **2014**, *43*, 1891–1894.
6. Long, Y.; Shi, Z.B.; Ding, Y.T.; Wang, J.; Xu, Y.; Fu, C.L. Growth and Characterization of Large size Terbium Gallium Garnet Single Crystal. *Piezoelectr. Acoustoopt.* **2016**, *38*, 433–436.
7. Hu, Q.Q.; Jia, Z.T.; Yin, Y.R.; Mu, W.X.; Zhang, J.; Tao, X.T. Crystal growth, thermal and optical properties of TSLAG magneto-optical crystals. *J. Alloys Comp.* **2019**, *805*, 496–501. [[CrossRef](#)]
8. Dou, R.Q.; Zhang, H.T.; Zhang, Q.L.; Zhuang, N.F.; Liu, W.P.; He, Y.; Chen, Y.Y.; Cheng, M.J.; Luo, J.Q.; Sun, D.L. Growth and properties of TSAG and TSLAG magneto-optical crystals with large size. *Opt. Mater.* **2019**, *96*, 109272. [[CrossRef](#)]
9. Ding, S.; Zhang, Q.; Liu, W.; Sun, G.; Sun, D. Crystal growth, defects, mechanical, thermal and optical properties of  $\text{Tb}_3\text{Sc}_2\text{Al}_3\text{O}_{12}$  magneto-optical crystal. *J. Cryst. Growth* **2018**, *483*, 110–114. [[CrossRef](#)]
10. Shimamura, K.; Kito, T.; Castel, E.; Latynina, A.; Kunihiro, N. Growth of  $\{\text{Tb}_3\}[\text{Sc}_{2-x}\text{Lu}_x](\text{Al}_3)\text{O}_{12}$  single crystals for visible-infrared optical isolators. *Cryst. Growth Des.* **2010**, *10*, 3466–3470. [[CrossRef](#)]
11. Villora, E.; Molin, P.; Nakamura, M.; Shimamura, K.; Hatanaka, T.; Funaki, A.; Naoe, K. Faraday rotator properties of  $\{\text{Tb}_3\}[\text{Sc}_{1.95}\text{Lu}_{0.05}](\text{Al}_3)\text{O}_{12}$ , a highly transparent terbium-garnet for visible-infrared optical isolators. *Appl. Phys. Lett.* **2011**, *99*, 011111. [[CrossRef](#)]
12. Le, C.C.; Li, Z.Y.; Mu, W.X.; Jia, Z.T.; Liu, L.J. 3D numerical design of the thermal field before seeding in an edge-defined film-fed growth system for  $\beta\text{-Ga}_2\text{O}_3$  ribbon crystals. *J. Cryst. Growth* **2019**, *506*, 83–90. [[CrossRef](#)]
13. Fainberg, J.; Leister, H.J. Finite volume multigrid solver for thermo-elastic stress analysis in anisotropic materials. *Comput. Methods Appl. Mech. Eng.* **1996**, *137*, 167–174. [[CrossRef](#)]
14. Ding, J.L.; Liu, L.J. The influence mechanism of melt flow instability on the temperature fluctuation on the crystal/melt interface during Czochralski silicon crystal growth. *Int. J. Heat Mass Tran.* **2019**, *142*, 118463. [[CrossRef](#)]
15. Ding, J.L.; Liu, L.J. Real-time prediction of crystal/melt interface shape during Czochralski crystal growth. *CrystEngComm* **2018**, *20*, 6925–6931. [[CrossRef](#)]
16. Chen, S.S.; Liu, W.K.; Wen, Z.C.; Liu, Y.; Jiang, F.M.; Xue, Z.Y.; Wei, X.; Li, W. Effects of Induced Current in Crystals on the Melt Flow and the Melt-Crystal Interface during Industrial 300 mm Czochralski Silicon Crystal Growth under a Transverse Magnetic Field. *Cryst. Growth Des.* **2023**, *23*, 4480–4490. [[CrossRef](#)]

17. Noghabi, O.A.; Hamdi, M.M.; Jomaa, M. Effect of crystal and crucible rotations on the interface shape of Czochralski grown silicon single crystals. *J. Cryst. Growth* **2011**, *318*, 173–177. [[CrossRef](#)]
18. Saadatirad, M.; Tavakoli, M.H.; Khodamoradi, H.; Masharian, S.R. Effect of the pulling, crystal and crucible rotation rate on the thermal stress and the melt–crystal interface in the Czochralski growth of germanium crystals. *CrystEngComm* **2021**, *23*, 6967. [[CrossRef](#)]

**Disclaimer/Publisher’s Note:** The statements, opinions and data contained in all publications are solely those of the individual author(s) and contributor(s) and not of MDPI and/or the editor(s). MDPI and/or the editor(s) disclaim responsibility for any injury to people or property resulting from any ideas, methods, instructions or products referred to in the content.